



Article

# Role of Mn<sup>2+</sup> Doping in the Preparation of Core-Shell Structured Fe<sub>3</sub>O<sub>4</sub>@upconversion Nanoparticles and Their Applications in T<sub>1</sub>/T<sub>2</sub>-Weighted Magnetic Resonance Imaging, Upconversion Luminescent Imaging and Near-Infrared Activated Photodynamic Therapy

Yang Luo <sup>†</sup>, Wei Zhang <sup>†</sup>, Zhengfang Liao, Shengnan Yang, Shengtao Yang , Xinhua Li, Fang Zuo <sup>\*</sup> and Jianbin Luo <sup>\*</sup>

College of Chemistry & Environment Protection Engineering, Southwest Minzu University, Chengdu 610041, China; polymerluoyang@163.com (Y.L.); w070812138@163.com (W.Z.); LiaoZfpolymer@163.com (Z.L.); yangsn1993@163.com (S.N.Y.); yangst@pku.edu.cn (S.T.Y.); lxh1905@126.com (X.L.)

<sup>\*</sup> Correspondence: polymerzf@swun.cn (F.Z.); luojb1971@163.com (J.L.); Tel.: +86-28-8552-3792 (F.Z.)

<sup>†</sup> These authors contributed equally to this work.

Received: 25 May 2018; Accepted: 22 June 2018; Published: 26 June 2018



**Abstract:** Core-shell (C/S) structured upconversion coated Fe<sub>3</sub>O<sub>4</sub> nanoparticles (NPs) are of great interest due to their potential as magnetic resonance imaging (MRI) and upconversion luminescent (UCL) imaging agents, as well as near-infrared activated photodynamic therapy (PDT) platforms. When C/S structured Fe<sub>3</sub>O<sub>4</sub>@Mn<sup>2+</sup>-doped NaYF<sub>4</sub>:Yb/Er NPs were prepared previously, well-defined C/S-NPs could not be formed without the doping of Mn<sup>2+</sup> during synthesis. Here, the role of Mn<sup>2+</sup> doping on the synthesis of core-shell structured magnetic-upconversion nanoparticles (MUCNPs) is investigated in detail. Core-shell-shell nanoparticles (C/S/S-MUCNPs) with Fe<sub>3</sub>O<sub>4</sub> as the core, an inert layer of Mn<sup>2+</sup>-doped NaYF<sub>4</sub> and an outer shell consisting of Mn<sup>2+</sup>-doped NaYF<sub>4</sub>:Yb/Er were prepared. To further develop C/S/S-MUCNPs applications in the biological field, amphiphilic poly(maleic anhydride-alt-1-octadecene) (C<sub>18</sub>PMH) modified with amine functionalized methoxy poly(ethylene glycol) (C<sub>18</sub>PMH-mPEG) was used as a capping ligand to modify the surface of C/S/S-MUCNPs to improve biocompatibility. UCL imaging, T<sub>1</sub>-weighted MRI ascribed to the Mn<sup>2+</sup> ions and T<sub>2</sub>-weighted MRI ascribed to the Fe<sub>3</sub>O<sub>4</sub> core of C/S/S-MUCNPs were then evaluated. Finally, chlorine e6 (Ce6) was loaded on the C/S/S-MUCNPs and the PDT performance of these NPs was explored. Mn<sup>2+</sup> doping is an effective method to control the formation of core-shell structured MUCNPs, which would be potential candidate as multifunctional nanoprobes for future T<sub>1</sub>/T<sub>2</sub>-weighted MR/UCL imaging and PDT platforms.

**Keywords:** Mn<sup>2+</sup>; Fe<sub>3</sub>O<sub>4</sub>; upconversion; core-shell-shell; MR/UCL imaging; PDT platforms

## 1. Introduction

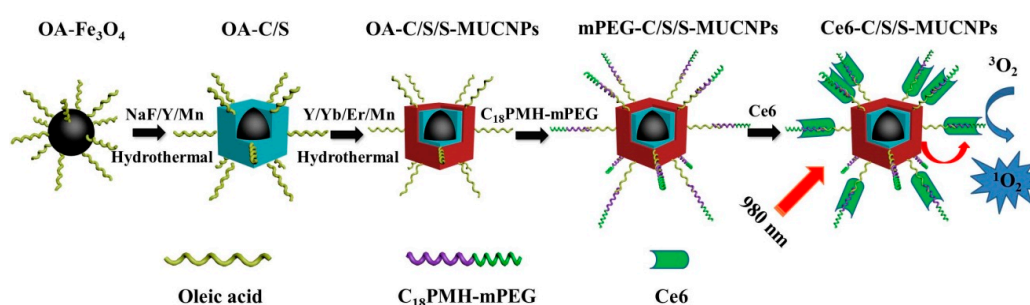
In recent years, a combination of magnetic iron oxides with upconversion to obtain magnetic-upconversion nanoparticles (MUCNPs) has received intensive attention in various biomedical fields. MUCNPs possess both useful magnetic properties and upconversion luminescent (UCL) properties. This allows them to be applied as nanoprobes for in vitro and in vivo dual-modal magnetic resonance imaging (MRI)/UCL imaging, providing high sensitivity/resolution fluorescence imaging and non-invasive and high spatial resolution MRI for real-time monitoring [1]. In addition to

bioimaging, MUCNPs have also been used for drug delivery and therapy in living cells and animals. Due to their deep penetration, UCL nanoparticles conjugated with photosensitizers have become important nanocarriers for photodynamic therapy (PDT) agents [2,3].

So far, several different methods have been developed to prepare MUCNPs, such as using mesoporous silica as an intermediate layer to combine UCNPs with  $\text{Fe}_3\text{O}_4$  NPs [4–6], polymer encapsulation [7,8], ligand crosslinking [9,10] and direct seed-nucleation [11–13]. This seed-growth method can be applied to construct MUCNPs by using one part as a seed onto which a second component can nucleate and grow [14,15]. The seed-growth method offers products with small sizes, homogeneous structures and tunable stoichiometry and can yield MUCNPs with core-shell (C/S) structures. On the other hand, transition metal ions, such as  $\text{Mn}^{2+}$ , are often used as dopants to regulate the morphology and fluorescence intensity of UCNPs, which also play a role in  $T_1$ -weighted MRI contrast agents.

Based on these works, we previously prepared  $\text{Mn}^{2+}$ -doped C/S-MUCNPs ( $\text{Fe}_3\text{O}_4$ @ $\text{Mn}^{2+}$ -doped  $\text{NaYF}_4$ :Yb/Er NPs) using seed-induced growth. In this previous study, the fluorescence intensity of MUCNPs decreased due to the existence of  $\text{Fe}_3\text{O}_4$ , which was caused by an energy transfer process [16]. The  $\text{Mn}^{2+}$  ions also play an important role in the formation of C/S-MUCNPs; if the  $\text{Mn}^{2+}$  ions are absent, MUCNPs cannot be obtained with high quality.

In the present work, we studied the effect of  $\text{Mn}^{2+}$  doping on the formation of C/S-MUCNPs. We prepared core-shell-shell (C/S/S) nanoparticles ( $\text{Fe}_3\text{O}_4$ @ $\text{Mn}^{2+}$ -doped  $\text{NaYF}_4$ @ $\text{Mn}^{2+}$ -doped  $\text{NaYF}_4$ :Yb/Er NPs) with  $\text{Fe}_3\text{O}_4$  as the core, an inert layer of  $\text{Mn}^{2+}$  doped  $\text{NaYF}_4$  and an outer shell of  $\text{Mn}^{2+}$ -doped  $\text{NaYF}_4$ :Yb/Er. We hypothesized that the inert layer of  $\text{Mn}^{2+}$ -doped  $\text{NaYF}_4$  could shield the  $\text{Fe}_3\text{O}_4$  core from the outer upconversion shell, which would decrease the quenching induced by the presence of  $\text{Fe}_3\text{O}_4$ . Furthermore,  $\text{Mn}^{2+}$ -doped UCNPs were then used as imaging agents and drug carriers for PDT. Amphiphilic poly(maleic anhydride-alt-1-octadecene) ( $\text{C}_{18}\text{PMH}$ ) modified with amine functionalized methoxy poly(ethylene glycol) ( $\text{C}_{18}\text{PMH}$ -mPEG), was then used to modify the C/S/S-MUCNPs in order to impart good biocompatibility. Finally, the obtained hydrophilic MUCNPs were used as contrast agents for  $T_1$ / $T_2$ -weighted MRI and UCL imaging as well as near-infrared (NIR) activated PDT agents. The overall synthesis procedure is illustrated in Scheme 1.



**Scheme 1.** Schematic representation of the formation of Ce6-C/S/S-MUCNPs and the near-infrared (NIR) targeting photosensitizer to generate singlet oxygen species for photodynamic therapy (PDT).

## 2. Materials and Methods

### 2.1. Materials

All starting chemicals were obtained from commercial supplies. Ferrous sulfate heptahydrate (reagent grade, 99%) were supplied by Jinshan Chemical Technology Co., Ltd (Chengdu, China). Yttrium nitrate hexahydrate (99.99%), Ytterbium nitrate (99.99%) and Erbium trinitrate pentahydrate (99.9%) were purchased by Best Chemical Reagent Co., Ltd (Chengdu, China). Oleic acid (OA) (technical grade, 98.0%), sodium fluoride (reagent grade, 98.0%), sodium hydroxide (reagent grade, 96%), ethanol (reagent grade, 99.7%), ferric trichloride hexahydrate (reagent grade, 99.0%),

manganese dichloride tetrahydrate (reagent grade, 98.0%), dimethyl sulfoxide (DMSO) were supplied by Kelong Chemical Technology Co., Ltd (Chengdu, China). Toluene (reagent grade, 99.5%), chloroform (reagent grade, 99.0%) and dichloromethane (reagent grade, 99.0%) were purchased from Ruijinte Chemical Technology Co., Ltd (Tianjin, China). Ammonia solution (reagent grade, 28%) and triethylamine (TEA) were supplied by Kelong Chemical Technology Co., Ltd. Poly(maleicanhydride-alt-1-octadecene) ( $C_{18}$ PMH) were supplied by Sigma-Aldrich Co., LLC. (Shanghai, China). Methoxy poly(ethylene glycol) amine (mPEG-NH<sub>2</sub>) were supplied by Aladdin company (Shanghai, China). 1-ethyl-3-(3-(dimethylamino)propyl) carbodiimide hydrochloride (EDC·HCl) and 1,3-Diphenylisobenzofuran (DPBF) were obtained from Best Chemical Reagent Co., Ltd. Chlorin e6 were supplied by Frontier Scientific (Logan, UT, USA).

### 2.2. Synthesis of OA Coated $Fe_3O_4@NaYF_4:xMn$ ( $x = 0, 30$ mol %) NPs

First, the hydrophobic OA coated  $Fe_3O_4$  NPs were prepared according to our previously reported procedure and then dispersed in toluene for use in the next step [17]. The as-prepared OA- $Fe_3O_4$  NPs were used as seeds and covered with shell according to our previously reported method [18]. In the case of  $Fe_3O_4@NaYF_4:xMn$  ( $x = 30$  mol %) NPs, as an example, 1.42 mL of 0.5 M  $MnCl_2$ , 3.31 mL of 0.5 M  $Y(NO_3)_3$  water solution were added to a mixture of NaOH (1.0 g), 5.0 mL toluene dispersion of OA- $Fe_3O_4$  (12 mg/mL), OA (16.72 mL) and ethanol (33.55 mL) under stirring. Then 10 mL of deionized water containing 0.68 g NaF was drop wisely added into the mixture. After vigorous stirring for 30 min, the colloidal solution was transferred into a 100 mL Teflon-lined autoclave (Guo wei technology limited, Chengdu, China), which was sealed and heated at 200 °C for 8 h and then the mixture was cooled down to room temperature. The final product was collected by magnetic-separation and then washed with ethanol and deionized water for several times. Finally, the obtained OA-coated  $Fe_3O_4@NaYF_4:xMn$  ( $x = 30$  mol %) NPs ( $G1-NaYF_4-Mn^{2+}$  MUCNPs) were dispersed in toluene.

### 2.3. Synthesis of OA Coated $Fe_3O_4@NaYF_4:18\%Yb/2\%Er/xMn$ ( $x = 0, 30$ mol %) NPs

The OA coated  $Fe_3O_4@NaYF_4:18\%Yb/2\%Er/xMn$  ( $x = 0, 30$  mol %) NPs were also prepared according to our previously reported method [18]. In the procedure, the obtained OA coated  $Fe_3O_4@NaYF_4:18\%Yb/2\%Er/xMn$  ( $x = 30$  mol %) NPs ( $G2-NaYF_4-Mn^{2+}$  MUCNPs) and OA coated  $Fe_3O_4@NaYF_4:18\%Yb/2\%Er/xMn$  ( $x = 0$  mol %) NPs ( $G2-NaYF_4$  MUCNPs) were dispersed in toluene.

### 2.4. Synthesis of OA Coated $Fe_3O_4@NaYF_4:xMn@NaYF_4:18\%Yb/2\%Er/xMn$ ( $x = 30$ mol %) Core/Inert Shell/Active Shell Structured MUCNPs

To form the second shell, the as-prepared  $G1-NaYF_4-Mn^{2+}$  MUCNPs were used as the nucleation seeds for growth of the active capping layer. The  $G1-NaYF_4-Mn^{2+}$  MUCNPs were used as seeds and covered with an active shell using a facile hydrothermal method according to our previously reported method [18]. The final product was collected by magnetic-separation and then washed with ethanol and deionized water for several times. Finally, the obtained OA- $Fe_3O_4@NaYF_4/xMn@NaYF_4:18\%Yb/2\%Er/xMn$  ( $x = 30$  mol %) NPs (OA-C/S/S-MUCNPs) were dispersed in chloroform.

### 2.5. Synthesis of mPEG-Functionalized $Fe_3O_4@NaYF_4:xMn@NaYF_4:18\%Yb/2\%Er/xMn$ ( $x = 30$ mol %) Core/Inert Shell/Active Shell Structured MUCNPs

The synthesis of mPEG- $Fe_3O_4@NaYF_4:xMn@NaYF_4:18\%Yb/2\%Er/xMn$  ( $x = 30$  mol %) NPs (mPEG-C/S/S-MUCNPs) was carried out according to a published method [19–21]. At first,  $C_{18}$ PMH-mPEG was synthesized according to a published protocol [22,23].  $C_{18}$ PMH-mPEG (15 mg) and OA coated  $Fe_3O_4@NaYF_4:xMn@NaYF_4:18\%Yb/2\%Er/xMn$  ( $x = 30$  mol %) NPs (15 mg) were dispersed separately in chloroform (10 mL) and then mixed together to obtain a homogeneous phase. The mixture was stirred for 2 h at room temperature. After magnetic separation, the black solid was

redispersed in 10 mL of water and the large aggregates were removed using a 0.22- $\mu\text{m}$  drainage membrane filter and mPEG-C/S/S-MUCNPs were stored at 4 °C.

#### 2.6. Synthesis of mPEG-Fe<sub>3</sub>O<sub>4</sub>@NaYF<sub>4</sub>:xMn@NaYF<sub>4</sub>:18%Yb/2%Er/xMn (x = 30 mol %) Core/Inert Shell/Active Shell Structured MUCNPs loaded with Ce6

According to a previously reported method [24], chlorin e6 (Ce6) molecules were loaded onto mPEG-C/S/S-MUCNPs via hydrophobic interactions. Briefly, 5 mg Ce6 was dissolved in 5 mL DMSO as the stock solution. Ce6 with the desired concentration (1 mg/mL) was added into mPEG-C/S/S-MUCNPs (0.5 mg/mL) aqueous solution. The mixture was placed at room temperature with continuous stirring, in the dark, overnight. The samples were removed after magnetic separation and washed 3 times with deionized water. The acquired mPEG-Fe<sub>3</sub>O<sub>4</sub>@NaYF<sub>4</sub>:xMn@NaYF<sub>4</sub>:18%Yb/2%Er/xMn (x = 30 mol %) NPs loaded with Ce6 (Ce6-C/S/S-MUCNPs) complex was redispersed in water by sonication and stored at 4 °C in the dark.

#### 2.7. Cytotoxicity Assay

The effect of mPEG-C/S/S-MUCNPs on cell viability was determined using MTT assay [25,26]. HeLa cells were seeded into 96-well plates at a density of  $1 \times 10^4$ /mL (200  $\mu\text{L}$  of fresh medium per well) and cultured at 37 °C and 5% CO<sub>2</sub>. The cell culture medium in each well was then replaced by 200  $\mu\text{L}$  of cell growth medium containing different concentrations of mPEG-C/S/S-MUCNPs (31.25, 62.50, 125, 250, 500  $\mu\text{g}/\text{mL}$ ). After incubation for 24 h, 200  $\mu\text{L}$  of MTT (0.5 mg/mL in a phosphate-buffered saline solution) was added to each well for another 4 h at 37 °C. The growth medium was removed gently using suction, 300  $\mu\text{L}$  of DMSO was added to each well as a solubilizing agent and the microplate was left at room temperature for 2 h.

#### 2.8. In Vivo UCL Imaging

Firstly, 50  $\mu\text{L}$  of mPEG-C/S/S-MUCNPs (500  $\mu\text{g}/\text{mL}$ ) were injected intradermally into the subcutaneous tissue of nude mice. The system includes two external adjustable CW 980 nm lasers (0–5 W) (Shanghai Connet Fiber Optics Co., Shanghai, China) sources and an Andor DU897 EMCCD as the signal collector. Images of luminescent signals were processed with the Kodak Molecular Imaging software (Rochester, NY, USA).

#### 2.9. In Vitro T<sub>1</sub>/T<sub>2</sub>-Weighted MRI

Initially, 1 mL of the mPEG-C/S/S-MUCNPs solution at different Mn<sup>2+</sup> concentrations or Fe concentrations were prepared before MRI. Both T<sub>1</sub>-weighted and T<sub>2</sub>-weighted magnetic resonance (MR) images were acquired using a 7.0 T MRI scanner (Bruker BioSpec 70/20 USR, Karlsruhe, Germany). The parameters refer to our previous method [27].

#### 2.10. Characterization

The morphology and size of the as-prepared MUCNPs were characterized by a Tecnai F20 Transmission Electron Microscopy (TEM) (Beijing, China) with an attached energy dispersive X-ray (EDX) spectroscopy system. Powder X-ray diffraction measurements were performed on a XD-6 diffractometer (Persee, Beijing, China) at a scanning rate of 8° min<sup>-1</sup> in the 2 $\theta$  range from 10° to 90° (Cu K $\alpha$  line  $\lambda = 0.154$  nm). The magnetic properties were assessed on a Vibrating Sample Magnetometer (VSM, HH-15, Nanjing, China) at 298 K under an applied magnetic field. The UCL spectra were performed by Hitachi F-4600 fluorescent spectrometer (Shanghai, China) using 980 nm diode laser. Fourier Transform Infrared Spectra (FTIR) were on Spectrum One (Chengdu, China) with KBr pellet in the spectral range of 4000 to 500 cm<sup>-1</sup>. SDTA 851C Thermogravimetric Analyzer (TGA) (Chengdu, China) was used to analysis of upconversion nanoparticles. An inductively coupled plasma mass spectrometry (ICP-MS) system (Shimadzu Corp., Kyoto, Japan) was used to analyze the element concentration of the MUCNPs.

### 3. Results

#### 3.1. Influence of $Mn^{2+}$ Doping on the Formation of Core-Shell Structured MUCNPs

In our previous work, the C/S-MUCNPs were prepared using a seeded-growth approach [18]. The obtained product precipitated in the absence of  $Mn^{2+}$  doping, indicating that the doping of  $Mn^{2+}$  plays an important role in the formation of C/S-MUCNPs with high-quality.

To explore the effect of  $Mn^{2+}$ -doping on the synthesis of C/S-MUCNPs, two groups of experiments were designed here; one group was synthesized in the presence of  $Y^{3+}$  with (G1-NaYF<sub>4</sub>- $Mn^{2+}$ ) or without  $Mn^{2+}$  doping (G1-NaYF<sub>4</sub>) and the other group was synthesized in the presence of  $Y^{3+}$ ,  $Yb^{3+}$  and  $Er^{3+}$  with (G2-NaYF<sub>4</sub>- $Mn^{2+}$ ) or without  $Mn^{2+}$  doping (G2-NaYF<sub>4</sub>). Figure 1 shows X-ray diffraction patterns (XRD) of the as-prepared products. Without  $Mn^{2+}$  doping, the product possesses a cubic phase (JCPDS No. 77-2042, marked with ■) and a hexagonal phase (JCPDS No. 16-0334, marked with \*) as shown in Figure 1a,c. Furthermore, the phase transformation from the coexistence of  $\alpha$  and  $\beta$ -phases to pure  $\alpha$ -phase was completed when 30 mol %  $Mn^{2+}$  doping was used, as shown in Figure 1b,d. The reflection peak intensity of  $Fe_3O_4$  contained in these products was relatively weak, likely because the magnetic materials in the composites occurred in a low concentration or had a low level of crystallization. The size and morphology of the as-prepared products were furthermore characterized by transmission electron microscopy (TEM). Figure 2a,c show TEM images of the obtained product prepared in the absence of  $Mn^{2+}$ , where the samples were aggregated and formed a mixture of NaYF<sub>4</sub> with  $\alpha$  and  $\beta$ -phases and isolated  $Fe_3O_4$  NPs. Figure 2b,d show TEM images of the samples prepared with 30 mol %  $Mn^{2+}$  doping, showing that high quality and uniform NPs with pure cubic phase structures were obtained.

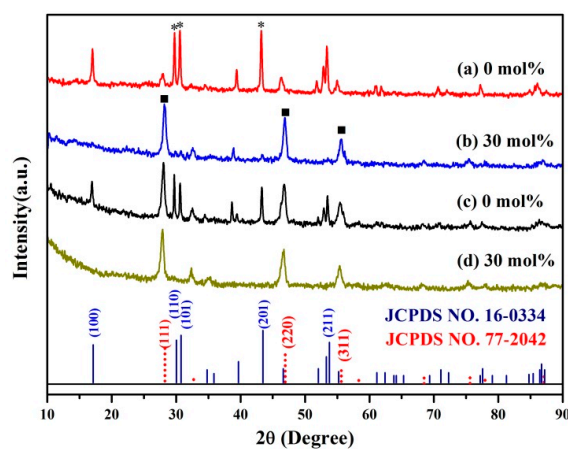


**Figure 1.** X-ray diffraction patterns of G1-NaYF<sub>4</sub> (a) and G1-NaYF<sub>4</sub>- $Mn^{2+}$  (b); G2-NaYF<sub>4</sub> (c) and G2-NaYF<sub>4</sub>- $Mn^{2+}$  (d). The diffraction peaks of the cubic phase are marked with ■ and peaks related to the hexagonal phase are marked with \*.

The TEM and XRD results indicated that if the upconversion part contained  $\beta$ -phases, the obtained product was deposited and low-quality products would be obtained. On the other hand, if the upconversion part featured only cubic phases, high-quality C/S-MUCNPs were obtained. Blower and co-workers demonstrated that C/S structured  $Fe_3O_4@NaYF_4$  (Yb/Er), could be formed by growing the (011) plane of cubic NaYF<sub>4</sub> on the (111) plane of  $Fe_3O_4$  with a rotation angle of 30° [13]. Meanwhile, Yan and co-workers showed that hexagonal NaYF<sub>4</sub> could not be directly formed on the surface of  $Fe_3O_4$  due to the lattice mismatch between  $Fe_3O_4$  and hexagonal NaYF<sub>4</sub> [28].

According to these previous works and the findings of this study,  $Mn^{2+}$  induced hexagonal-to-cubic phase transformations and the formed cubic phase grew on the surface of  $Fe_3O_4$  to obtain MUCNPs with a C/S structured.

To determine why the precipitation only takes place in the absence of  $\text{Mn}^{2+}$ , additional experiments were conducted in which only NaF was introduced into this system in the presence of oleic acid coated  $\text{Fe}_3\text{O}_4$  (OA- $\text{Fe}_3\text{O}_4$ ) NPs, precipitating the obtained product. X-ray photoelectron spectra (XPS) were then used to examine the composition of the precipitated product. As shown in Figure S1, a peak at 685.42 eV assigned to F-1s was found in the XPS spectra, indicating that  $\text{F}^-$  ions were absorbed onto the surface of  $\text{Fe}_3\text{O}_4$  NPs. According to these results, the  $\text{F}^-$  ions likely induce the desorption of OA bound onto the  $\text{Fe}_3\text{O}_4$ , in the presence of  $\text{Mn}^{2+}$ , causing nucleation and growth to occur on the surface of  $\text{Fe}_3\text{O}_4$ , followed by OA molecules being absorbed on the formed upconversion shell to stabilize the C/S-MUCNPs. Without  $\text{Mn}^{2+}$ , the rare earth ions would nucleate and grow into isolated UCNPs with lattice mismatch between  $\text{Fe}_3\text{O}_4$  and hexagonal  $\text{NaYF}_4$  and the  $\text{Fe}_3\text{O}_4$  NPs would aggregate and deposit due to the loss of stabilization provided by OA.

According to these results, the mechanism of the C/S-MUCNPs synthesis could be described as follows. The addition of NaF induced the desorption of OA molecules from the surface of  $\text{Fe}_3\text{O}_4$  NPs and then  $\text{Mn}^{2+}$  induced the nucleation and growth of the upconversion shell on the  $\text{Fe}_3\text{O}_4$  NPs, which resulted in the formation of C/S-MUCNPs stabilized by OA molecules. The proposed synthesis mechanism is illustrated in Scheme S1.

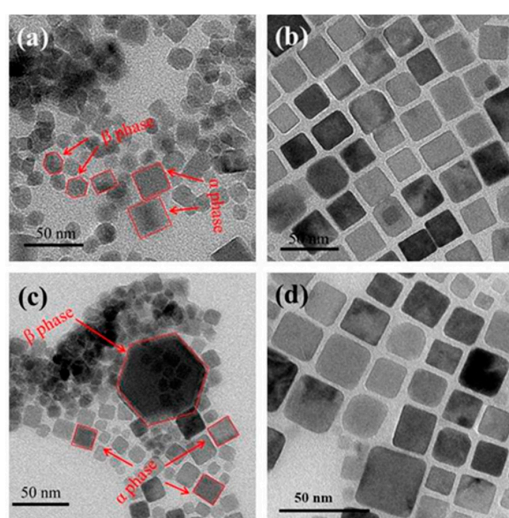


**Figure 2.** Transmission electron microscopy (TEM) images of G1- $\text{NaYF}_4$  (a) and G1- $\text{NaYF}_4\text{-Mn}^{2+}$  (b); G2- $\text{NaYF}_4$  (c) and G2- $\text{NaYF}_4\text{-Mn}^{2+}$  (d).

### 3.2. Preparation of Core/Inert Shell/Active Shell Structured MUCNPs

As discussed previously, an inert layer between  $\text{Fe}_3\text{O}_4$  NPs and luminescent shells in C/S structured luminescent and magnetic NPs could decrease the quenching of luminescence by the  $\text{Fe}_3\text{O}_4$  core. Core/inert shell/active shell structured MUCNPs were designed in this study, where  $\text{Fe}_3\text{O}_4$  NPs were coated by an inert shell of  $\text{Mn}^{2+}$ -doped  $\text{NaYF}_4$ , onto which the active UCL shell made of  $\text{Mn}^{2+}$  doped  $\text{NaYF}_4\text{:Yb/Er}$  was formed. In the following description, C/S/S-MUCNPs refers to the core/inert shell/active shell structured MUCNPs. The composition and structure of the C/S/S-MUCNPs were characterized by XRD and TEM, respectively. Figure S2 shows the XRD spectra of the C/S/S-MUCNPs, where the diffraction peaks were indexed to cubic-phase  $\text{NaYF}_4$  (JCPDS card No. 77-2042). Figure 3a shows TEM images of the C/S/S-MUCNPs, compared with that of the C/S structured  $\text{Fe}_3\text{O}_4\text{@Mn}^{2+}$ -doped  $\text{NaYF}_4$  NPs. The size was increased, indicating the formation of another shell on the inert shell of  $\text{Mn}^{2+}$ -doped  $\text{NaYF}_4$ . The fringe distances, measured using high resolution TEM (HRTEM) (Figure 3b), were 4.85 Å and 2.73 Å for the two types of grains, which matched well with the known lattice constants for  $\text{Fe}_3\text{O}_4$  and cubic  $\text{NaYF}_4$  phases, respectively. This confirms the successful coating of  $\text{Fe}_3\text{O}_4$  with a cubic upconversion shell.

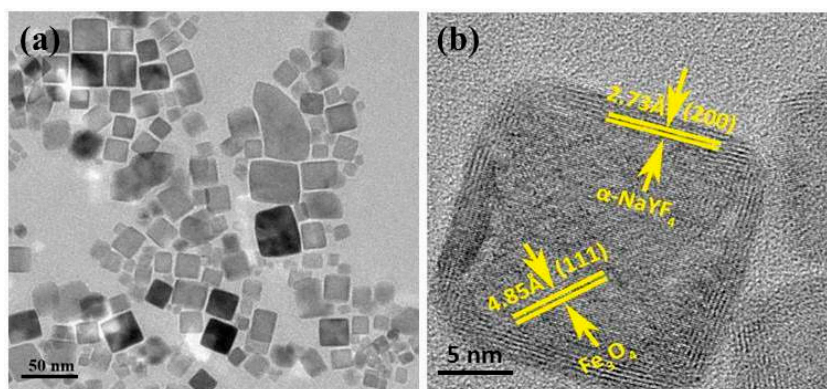


Figure 3. TEM image (a) and HRTEM image (b) of C/S/S-MUCNPs.

To further confirm the formation of the composite structure, energy dispersive X-ray (EDX) was conducted, where the results are shown in Figure 4. The EDX result clearly indicated that Fe, F, Na, Y, Yb, Er and Mn were detected in the central region, while no Fe signal was obtained from the shell part. The data indicated that C/S/S-MUCNPs magnetic-fluorescent nanocomposites were successfully prepared. Other signals came from the TEM grid.

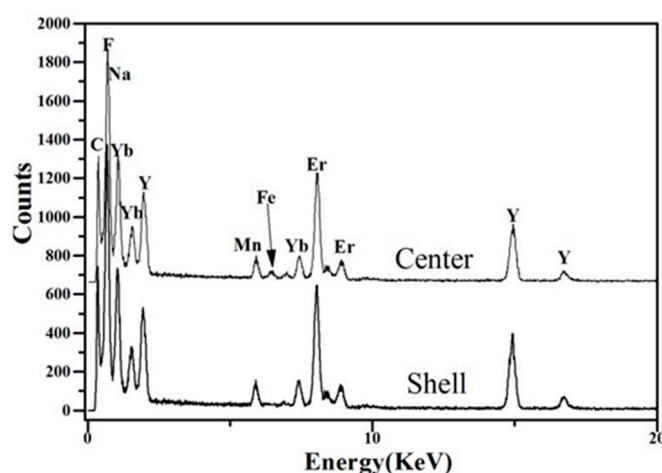
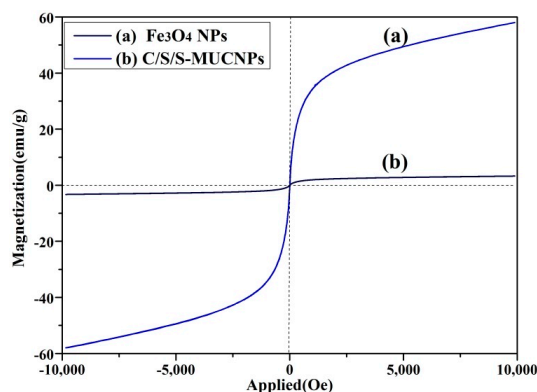


Figure 4. EDX analysis of the central and shell region of C/S/S-MUCNPs.

The magnetic properties of the C/S/S-MUCNPs and original  $\text{Fe}_3\text{O}_4$  NPs were then characterized with a VSM magnetometer. After the formation of the C/S/S-MUCNPs, the saturation magnetization was significantly decreased to  $3.85 \text{ emu}\cdot\text{g}^{-1}$  (Figure 5). This phenomenon was mainly caused by the presence of a high proportion of upconversion in the composite NPs. Fortunately, both the C/S/S-MUCNPs and the original  $\text{Fe}_3\text{O}_4$  nanoparticles display superparamagnetic behavior (zero coercivity and resonance), which is crucial for use in biomedicine and biotechnology applications [29]. In the future, we plan to carry out a detailed study to improve the saturation magnetization of MUCNPs.



**Figure 5.** Room-temperature magnetic hysteresis loop for  $\text{Fe}_3\text{O}_4$  NPs (a) and C/S/S-MUCNPs (b).

The optical properties of the C/S/S-MUCNPs were also investigated. A higher UCL emission intensity was clearly observed for C/S/S-MUCNPs compared to the C/S-MUCNPs (Figure 6), due to the existence of the inert shell which prevented the fluorescence from being quenched by  $\text{Fe}_3\text{O}_4$  [30]. The UCL spectra of C/S/S-MUCNPs in chloroform (Figure 6) exhibited two peaks at 550 nm (green emission peak) and 660 nm (red emission peak), where the red to green intensity ratio (IR/IG) was 3.13. The intense red light (650–670 nm) luminescence was ascribed to the presence of  $\text{Mn}^{2+}$  [31,32].

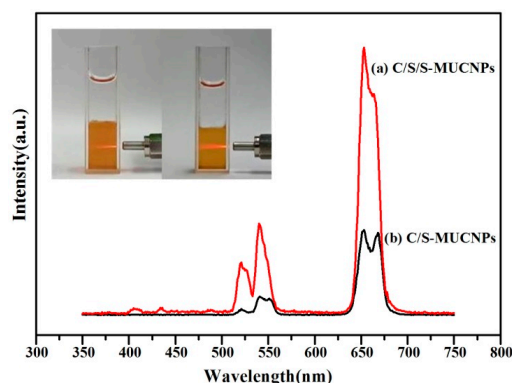


**Figure 6.** Upconversion emission spectra of C/S/S-MUCNPs (a) and C/S-MUCNPs (b). The inset shows photographic images of the chloroform solution of MUCNPs under 980 nm irradiation, C/S-MUCNPs (left) and C/S/S-MUCNPs (right).

The C/S/S-MUCNPs described above, which were inevitably covered with OA, were converted to a water-soluble form by coating them with amphiphilic polymer (poly(maleic anhydride-alt-1-octadecene) modified with methoxy poly(ethylene glycol) amine ( $\text{C}_{18}\text{PMH-mPEG}$ )), as shown in Figure S3. The appearance of characteristic peaks associated with the PEG chain at  $1107$  and  $952\text{ cm}^{-1}$  in the Fourier transform infrared (FTIR) spectra of PEGylated NPs (Figure S3) and a mass loss of up to 30.7% starting from  $>200\text{ }^\circ\text{C}$  on thermogravimetric curves (Figure S4), confirmed the coating of  $\text{C}_{18}\text{PMH-mPEG}$ . As shown in Figure S2, the XRD spectra indicated that the  $\text{C}_{18}\text{PMH-mPEG}$  coated C/S/S-MUCNPs (mPEG-C/S/S-MUCNPs) maintained a cubic phase structure (JCPDS Card No. 77-2042). In addition, the mPEG-C/S/S-MUCNPs were separated from each other without observable aggregation, suggesting that they were effectively stabilized in the aqueous solution (Figure S5).

### 3.3. In Vitro UCL Imaging and In Vitro $T_1/T_2$ -Weighted MRI Imaging

Prior to in vitro and in vivo biological applications, the cytotoxicity of the obtained mPEG-C/S/S-MUCNPs was measured using an MTT assay, an approach widely used to measure

mitochondria activity to quantify cell growth or cell death [33]. The viability of the untreated cells was assumed to be 100%. Figure 7 shows the cell viability after 24 h of incubation with the mPEG-C/S/S-MUCNPs at different concentrations from 31.25 to 500  $\mu\text{g}\cdot\text{mL}^{-1}$ . After 24 h of incubation at a concentration of 500  $\mu\text{g}\cdot\text{mL}^{-1}$ , the cells viability was approximately 81%. These results indicate that the prepared mPEG-C/S/S-MUCNPs exhibit low toxicity.

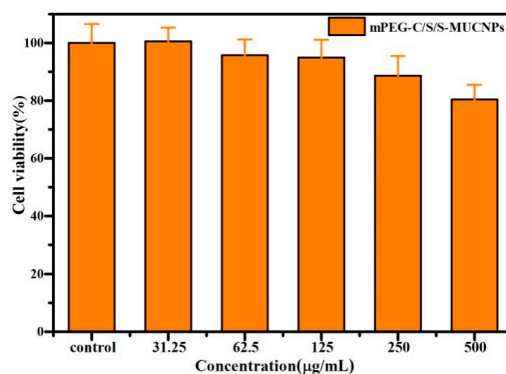


**Figure 7.** In vitro cytotoxicity of mPEG-C/S/S-MUCNPs against HeLa cells at different concentrations after 24 h incubation.

UCL imaging is a non-invasive and sensitive method to visualize morphological details of biological samples [34–36]. To verify the capacity of the mPEG-C/S/S-MUCNPs for UCL imaging, we injected mPEG-C/S/S-MUCNPs into the thighs of mice. UCL imaging was achieved from the injected sites using an EMCCD camera, where excitation was provided by a CW infrared laser at 980 nm and UCL signals were collected at  $660 \pm 12$  nm. The strong NIR UCL signal was detected at the mice thigh by the in vivo Maestro (CRI) imaging system upon excitation at 980 nm (Figure 8b). The overlay image (Figure 8c) with high signal-to-noise ratio (SNR = 18.26) further confirmed that the mPEG-C/S/S-MUCNPs were an excellent probe for in vivo NIR UCL imaging.

The elemental composition of mPEG-C/S/S-MUCNPs was analyzed by ICP-MS, where the Fe/Mn molar ratio was estimated to be 2.38:1. In order to evaluate the ability of mPEG-C/S/S-MUCNPs as a  $T_1$ – $T_2$  dual modal MRI agent, the transverse relaxivity ( $r_2$ ) and longitudinal relaxivity ( $r_1$ ) were determined by plotting the inverse relaxation time against the Fe and Mn concentration, respectively. The  $r_1$  was  $5.24 \text{ mM}^{-1} \text{ s}^{-1}$  which was calculated from the curve of  $1/T_1$  versus the  $\text{Mn}^{2+}$  concentration (Figure 9a), Meanwhile, the  $r_2$  was calculated to be  $22.48 \text{ mM}^{-1} \text{ s}^{-1}$  (Figure 9b). These results suggested that the NPs could be used for both  $T_1$ - and  $T_2$ -weighted MR imaging. In future studies, we will investigate the effect of Mn and Fe contents and the interaction between Mn-doped  $\text{NaYF}_4$  and  $\text{Fe}_3\text{O}_4$  on the  $r_2/r_1$  ratio to make these MUCNPs viable for use in MRI imaging.

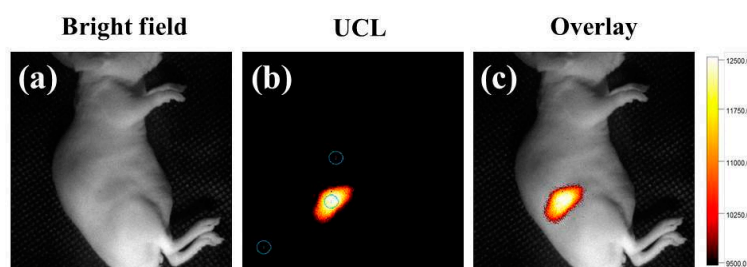


**Figure 8.** In vivo upconversion luminescence (UCL) imaging. Bright field image (a); UCL image after injection with mPEG-C/S/S-MUCNPs (0.5 mg/mL, 50  $\mu\text{L}$ ) under irradiation at 980 nm (power density of  $300 \text{ mW}/\text{cm}^2$ ,  $\lambda$  emission =  $660 \pm 12$  nm) (b); merged image of bright field image and UCL signal (c).

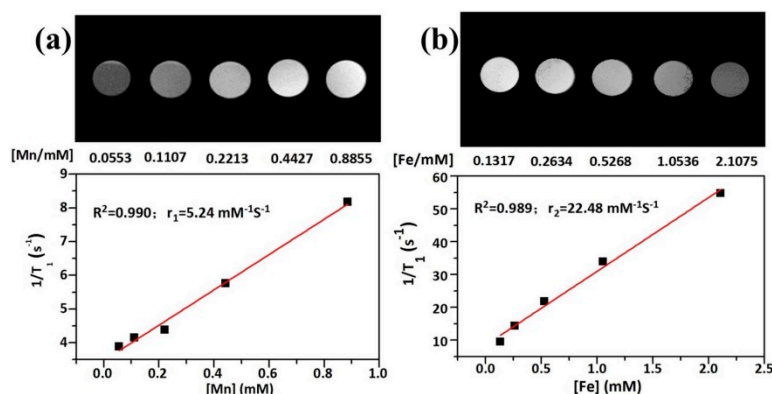


**Figure 9.** In vitro  $T_1$ -weighted image of mPEG-C/S/S-MUCNPs and a relaxivity plot of  $r_1$  vs. Mn contents (a). In vitro  $T_2$ -weighted image of mPEG-C/S/S-MUCNPs and a relaxivity plot of  $r_2$  vs. Fe contents (b).

### 3.4. Evaluation of PDT Performance of C/S/S-MUCNPs Loaded with Ce6

To demonstrate the feasibility of using mPEG-C/S/S-MUCNPs loaded with Ce6 (Ce6-C/S/S-MUCNPs) in PDT, Ce6 was conjugated to C/S/S-MUCNPs, as the black emission from the MUCNPs matched well with the absorption peak of Ce6 (Figure S6). To analyze the energy transfer between MUCNPs and Ce6, we measured the UC emission spectra of MUCNPs-Ce6 complexes using 980 nm excitation (Figure 10). The intensity ratio of the green emission peak (IG) to the red emission peak (IR) was about 2.2:1 for Ce6-C/S/S-MUCNPs. However, the IG:IR was only 1:2.8 for mPEG-C/S/S-MUCNPs due to resonance energy transfer from the MUCNPs to the nearby Ce6 molecules, which had an absorption peak at exactly 660 nm [37,38].

Singlet oxygen is thought to be the major cytotoxic species that causes cell death through the so-called type II mechanism [39,40]. Herein, a singlet-oxygen chemical probe, 1,4-diphenyl-2,3-benzofuran (DPBF), was chosen to evaluate the  $^1\text{O}_2$  generation capability of Ce6-C/S/S-MUCNPs, owing to the fact that DPBF can react irreversibly with generated  $^1\text{O}_2$ , leading to a decreased intensity of the DPBF absorption (around 410 nm) [41,42]. The changes in the absorption spectra of DPBF in the presence of Ce6-C/S/S-MUCNPs after different irradiation times are shown in Figure 11a. Control tests were carried out to confirm that the decrease in the absorption of DPBF was induced by singlet oxygen (Figure 11b). In the presence of Ce6-C/S/S-MUCNPs, the DPBF absorption at 410 nm dramatically decreased under 980 nm irradiation (Figure 11a,b), thereby suggesting that these NPs were highly efficient in the generation of reactive  $^1\text{O}_2$ . In contrast, there were no obvious decreases in DPBF absorbance for solutions containing mPEG-C/S/S-MUCNPs or free Ce6 (Figure 11b). The effective  $^1\text{O}_2$ -generating capability of Ce6-C/S/S-MUCNPs under NIR radiation makes them viable for NIR-induced PDT applications.

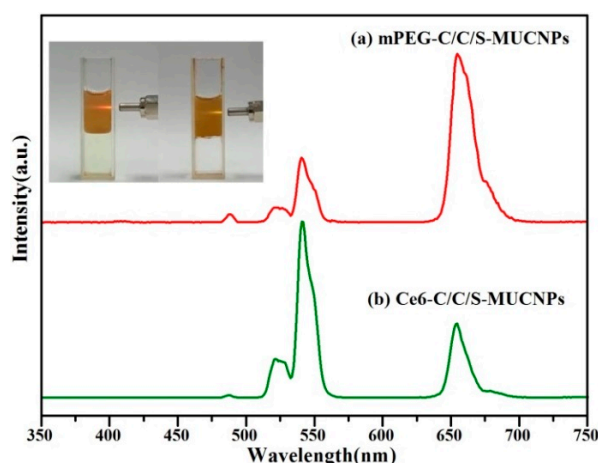


**Figure 10.** UCL spectra of mPEG-C/S/S-MUCNPs (a) and Ce6-C/S/S-MUCNPs (b) under the excitation of a 980 nm diode laser.

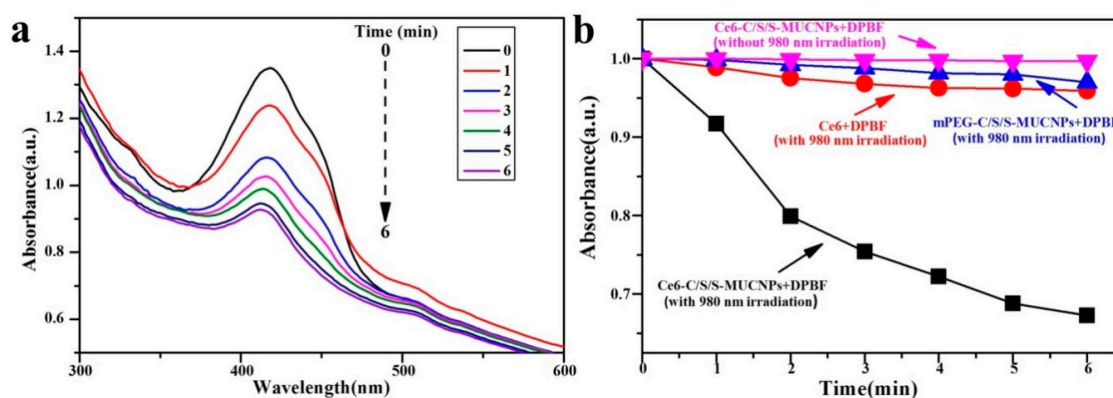


**Figure 11.** Absorption spectra of 1,3-Diphenylisobenzofuran (DPBF) under NIR irradiation in aqueous dispersion of Ce6-C/S/S MUCNPs ( $100 \mu\text{g}\cdot\text{mL}^{-1}$ ) (a); Consumption of DPBF over time (black); others were control experiments without UCNPs or NIR, respectively (b).

The PDT efficiency of Ce6-C/S/S-MUCNPs was preliminarily evaluated on HeLa cancer cells using the standard MTT assay. As shown in Figure 12, no significant cytotoxicity was observed after treatment with Ce6-C/S/S-MUCNPs in the absence of irradiation. In contrast, the cell viability of Ce6-C/S/S-MUCNPs ( $300 \mu\text{g}/\text{mL}$ ) decreased to approximately 44% after a 10-min laser irradiation ( $0.3 \text{ W}/\text{cm}^2$ ). This demonstrates that these NPs can exert severe toxicity to HeLa cells upon 980 nm laser irradiation. No reduction in cell viability was noticed for cells incubated with bare NPs in the presence of NIR irradiation (Figure 12), indicating that bare NPs with irradiation did not produce cancer cell-killing singlet oxygen. These results clearly demonstrate the feasibility of Ce6-C/S/S-MUCNPs as PDT agents.

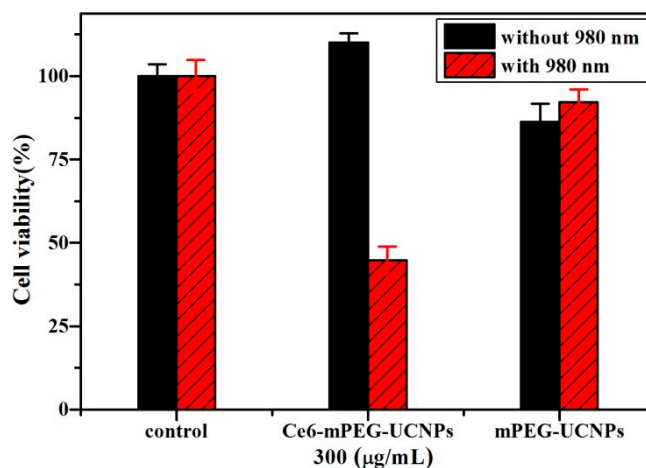


**Figure 12.** Viability of HeLa cells treated with mPEG- and Ce6-C/S/S MUCNPs at 300 µg/mL with and without (0.3 W/cm<sup>2</sup>) 980 nm irradiation.

#### 4. Conclusions

In summary, Mn<sup>2+</sup> doping was confirmed to be crucial for the formation of core-shell structured MUCNPs, as the doping of Mn<sup>2+</sup> could induce hexagonal-to-cubic phase transformations, where only the formed cubic phase can grow on the surface of Fe<sub>3</sub>O<sub>4</sub> NPs. Core/inert shell/active shell structured MUCNPs were then prepared, where Fe<sub>3</sub>O<sub>4</sub> NPs were coated by the inert shell of Mn<sup>2+</sup>-doped NaYF<sub>4</sub>, on which an active UCL shell made of Mn<sup>2+</sup>-doped NaYF<sub>4</sub>:Yb/Er was formed. The inert shell prevented the UCL from being quenched by Fe<sub>3</sub>O<sub>4</sub>. Furthermore, water-dispersible C/S/S-MUCNPs were obtained by coating with an amphiphilic polymer (C<sub>18</sub>PMH-mPEG), which exhibited good biocompatibility. Moreover, the prepared C<sub>18</sub>PMH-mPEG coated C/S/S-MUCNPs could be used for in vivo UCL imaging with a signal-to-noise ratio of 18.26. The C/S/S-MUCNPs were also used as dual-mode T<sub>1</sub>/T<sub>2</sub>-weighted MRI agent because of the co-existence of Fe<sub>3</sub>O<sub>4</sub> and Mn<sup>2+</sup> in the NPs, with an r<sub>1</sub> value of 5.24 mM<sup>-1</sup> s<sup>-1</sup> and r<sub>2</sub> value of 22.48 mM<sup>-1</sup> s<sup>-1</sup>. On the other hand, the main UCL band at 654–674 nm was matched with the excitation wavelength of the Ce6 photosensitizer, by which singlet oxygen species were generated to kill cancer cells. Under irradiation by 980 nm laser for 10 min, the cell death of HeLa cells incubated with Ce6-C/S/S-MUCNPs (300 µg·mL<sup>-1</sup>) could reach approximately 56%. Therefore, the as-prepared C/S/S-MUCNPs are thought to be good multifunctional agents for T<sub>1</sub>/T<sub>2</sub>-weighted MR/UCL imaging and PDT platforms for cancer treatment.

**Supplementary Materials:** The following are available online at <http://www.mdpi.com/2079-4991/8/7/466/s1>, Scheme S1: Proposed synthetic mechanism for the formation of Fe<sub>3</sub>O<sub>4</sub>@NaYF<sub>4</sub> NPs, Figure S1: XPS spectra of Fe<sub>3</sub>O<sub>4</sub> NPs treated by hydrothermal process in the presence of NaF, Figure S2: X-ray diffraction patterns of OA-C/S/S-MUCNPs (a) and mPEG-C/S/S-MUCNPs (b), Figure S3: FTIR spectra of OA-C/S/S-MUCNPs (a) and mPEG-C/S/S-MUCNPs (b), Figure S4: TGA curves of OA-C/S/S-MUCNPs (a) and mPEG-C/S/S-MUCNPs (b), Figure S5: TEM images of OA-C/S/S-MUCNPs (a) and mPEG-C/S/S-MUCNPs (b), Figure S6: UV-Vis absorbance spectrum of Ce6-C/S/S-MUCNPs (a), Ce6 (b), and mPEG-C/S/S-MUCNPs (c).

**Author Contributions:** Conceptualization, F.Z. and J.B.L.; Investigation, Y.L., W.Z., S.N.Y., S.T.Y., F.Z. and J.B.L.; Methodology, Y.L., W.Z., Z.F.L., F.Z. and J.B.L.; Writing—original draft, Y.L. and W.Z.; Writing—review & editing, X.H.L., F.Z. and J.B.L.

**Funding:** This research was funded by the National Natural Science Foundation of China (Grant number 51273220) and the Functional Polymer Innovation Team Project, Southwest University for Nationalities (No. 14CXTD04).

**Acknowledgments:** The authors thank Fuyou Li, Wei Feng and Cong Cao from FuDan University, who gave many instructions on UCL imaging. We would like to thank Editage [[www.editage.cn](http://www.editage.cn)] for English language editing.

**Conflicts of Interest:** The authors declare no conflict of interest.

## References

1. Zhang, L.; Wang, Y.S.; Yang, Y.; Zhang, F.; Dong, W.F.; Zhou, S.Y.; Pei, W.H.; Chen, H.D.; Sun, H.B. Magnetic/upconversion luminescent mesoparticles of  $\text{Fe}_3\text{O}_4@ \text{LaF}_3:\text{Yb}^{3+}, \text{Er}^{3+}$  for dual-modal bioimaging. *Chem. Commun.* **2012**, *48*, 11238–11240. [[CrossRef](#)] [[PubMed](#)]
2. Xu, F.L.; Liu, M.X.; Li, X.; Xiong, Z.J.; Cao, X.Y.; Shi, X.Y.; Guo, R. Loading of indocyanine green within polydopamine-coated laponite nanodisks for targeted cancer photothermal and photodynamic therapy. *Nanomaterials* **2018**, *8*, 347. [[CrossRef](#)] [[PubMed](#)]
3. Nancy, L.O.; Rachel, L.M.; Irina, B. The role of apoptosis in response to photodynamic therapy: What, where, why and how. *Photochem. Photobiol. Sci.* **2002**, *1*, 1–21. [[CrossRef](#)]
4. Darbandi, M.; Nann, T. One-pot synthesis of  $\text{YF}_3@ \text{silica}$  core/shell nanoparticles. *Chem. Commun.* **2006**, 776–778. [[CrossRef](#)] [[PubMed](#)]
5. Gai, S.L.; Yang, P.P.; Li, C.X.; Wang, W.X.; Dai, Y.L.; Niu, N.; Lin, J. Synthesis of magnetic, up-conversion luminescent and mesoporous core-shell-structured nanocomposites as drug carriers. *Adv. Funct. Mater.* **2010**, *20*, 1166–1172. [[CrossRef](#)]
6. Ansari, A.A.; Yadav, R.; Rai, S.B. Enhanced luminescence efficiency of aqueous dispersible  $\text{NaYF}_4:\text{Yb}/\text{Er}$  nanoparticles and the effect of surface coating. *RSC Adv.* **2016**, *6*, 22074–22082. [[CrossRef](#)]
7. Cheung, E.N.M.; Alvares, R.D.A.; Oakden, W.; Chaudhary, R.; Hill, M.L.; Pichaandi, J.Y.; Mo, G.C.H.; Yip, C.; Macdonald, P.M.; Stanisz, G.J.; et al. Polymer-stabilized lanthanide fluoride nanoparticle aggregates as contrast agents for magnetic resonance imaging and computed tomography. *Chem. Mater.* **2010**, *22*, 4728–4739. [[CrossRef](#)]
8. Jana, N.R.; Patra, P.K.; Saha, A.; Basiruddin, S.K.; Pradhan, N. Imidazole based biocompatible polymer coating in deriving <25 nm functional nanoparticle probe for cellular imaging and detection. *J. Phys. Chem. C* **2009**, *113*, 21484–21492. [[CrossRef](#)]
9. Jiang, S.; Win, K.Y.; Liu, S.H.; Teng, C.P.; Zheng, Y.G.; Han, M.Y. Surface-functionalized nanoparticles for biosensing and imaging-guided therapeutics. *Nanoscale* **2013**, *5*, 3127–3148. [[CrossRef](#)] [[PubMed](#)]
10. Feng, W.; Han, C.M.; Li, F.Y. Upconversion-nanophosphor-based functional nanocomposites. *Adv. Mater.* **2013**, *25*, 5287–5303. [[CrossRef](#)] [[PubMed](#)]
11. Huang, Z.Y.; Gao, H.P.; Mao, Y.L. Understanding the effect of  $\text{Mn}^{2+}$  on  $\text{Yb}^{3+}/\text{Er}^{3+}$  upconversion and obtaining a maximum upconversion fluorescence enhancement in inert-core/active-shell/inert-shell structures. *RSC Adv.* **2016**, *6*, 83321–83327. [[CrossRef](#)]
12. Zeng, L.Y.; Xiang, L.C.; Ren, W.Z.; Zheng, J.J.; Li, T.H.; Chen, B.; Zhang, J.C.; Mao, C.W.; Li, A.G.; Wu, A.G. Multifunctional photosensitizer-conjugated core-shell  $\text{Fe}_3\text{O}_4@ \text{NaYF}_4:\text{Yb}/\text{Er}$  nanocomplexes and their applications in  $T_2$ -weighted magnetic resonance/upconversion luminescence imaging and photodynamic therapy of cancer cells. *RSC Adv.* **2013**, *3*, 13915–13925. [[CrossRef](#)]
13. Cui, X.J.; Mathe, D.; Kovács, N.; Horváth, I.; Jauregui-Osoro, M.; Rosales, R.T.M.; Mullen, G.E.D.; Wong, W.; Yan, Y.; Krüger, D.; et al. Synthesis, characterization and application of core-shell  $\text{Co}_{0.16}\text{Fe}_{2.84}\text{O}_4@ \text{NaYF}_4(\text{Yb}, \text{Er})$  and  $\text{Fe}_3\text{O}_4@ \text{NaYF}_4(\text{Yb}, \text{Tm})$  nanoparticle as trimodal (MRI, PET/SPECT and Optical) imaging agents. *Bioconj. Chem.* **2016**, *27*, 319–328. [[CrossRef](#)] [[PubMed](#)]
14. Gu, H.W.; Zheng, R.K.; Zhang, X.X.; Xu, B. Facile one-pot synthesis of bifunctional heterodimers of nanoparticles: A conjugate of quantum dot and magnetic nanoparticles. *J. Am. Chem. Soc.* **2004**, *126*, 5664–5665. [[CrossRef](#)] [[PubMed](#)]
15. Kwon, K.W.; Shim, M.  $\gamma\text{-Fe}_2\text{O}_3/\text{II-VI}$  sulfide nanocrystal heterojunctions. *J. Am. Chem. Soc.* **2005**, *127*, 10269–10275. [[CrossRef](#)] [[PubMed](#)]
16. Moscoso-Londoño, O.; Ospina, C.; Brito, H.F.; Javed, Y.; Felinto, M.C.F.C.; Menezes, A.S.; Knobel, M.; Sharma, S.K. Building block magneto-luminescent nanomaterials of iron-oxide/ $\text{ZnS}@ \text{LaF}_3:\text{Ce}^{3+}, \text{Gd}^{3+}, \text{Tb}^{3+}$  with green emission. *J. Mater. Chem. C* **2017**, *5*, 2282–2290. [[CrossRef](#)]
17. An, P.; Zuo, F.; Wu, Y.P.; Zhang, J.H.; Zheng, Z.H.; Ding, X.B.; Peng, Y.X. Fast synthesis of dopamine-coated  $\text{Fe}_3\text{O}_4$  nanoparticles through ligand-exchange method. *Chin. Chem. Lett.* **2012**, *23*, 1099–1102. [[CrossRef](#)]
18. Qin, Z.L.; Du, S.N.; Luo, Y.; Liao, Z.J.; Zuo, F.; Luo, J.B.; Liu, D. Hydrothermal synthesis of superparamagnetic and red luminescent bifunctional  $\text{Fe}_3\text{O}_4@ \text{Mn}^{2+}$ -doped  $\text{NaYF}_4:\text{Yb}/\text{Er}$  core@shell monodisperse nanoparticles and their subsequent ligand exchange in water. *Appl. Surf. Sci.* **2016**, *378*, 174–180. [[CrossRef](#)]

19. Wei, R.; Wei, Z.; Sun, L.; Zhang, J.Z.; Liu, J.; Ge, X.; Shi, L. Nile red derivative-modified nanostructure for upconversion luminescence sensing and intracellular detection of Fe<sup>3+</sup> and MR imaging. *ACS Appl. Mater. Interfaces* **2016**, *8*, 400–410. [[CrossRef](#)] [[PubMed](#)]
20. Chang, H.J.; Xie, J.; Zhao, B.Z.; Liu, B.T.; Xu, S.L.; Ren, N.; Xie, X.J.; Huang, L.; Huang, W. Rare earth ion-doped upconversion nanocrystals: Synthesis and surface modification. *Nanomaterials* **2015**, *5*, 1–25. [[CrossRef](#)] [[PubMed](#)]
21. Wu, Y.Y.; Gao, D.Y.; Zhang, P.F.; Li, C.S.; Wan, Q.; Chen, C.; Gong, P.; Gao, G.H.; Sheng, Z.H.; Cai, L.T. Iron oxide nanoparticles protected by NIR-active multidentate-polymers as multifunctional nanoprobe for NIRF/PA/MR trimodal imaging. *Nanoscale* **2016**, *8*, 775–779. [[CrossRef](#)] [[PubMed](#)]
22. Prencipe, G.; Tabakman, S.M.; Welsher, K.; Liu, Z.; Goodwin, A.P.; Zhang, L.; Henry, J.; Dai, H.J. PEG branched polymer for functionalization of nanomaterials with ultralong blood circulation. *J. Am. Chem. Soc.* **2009**, *131*, 4783–4787. [[CrossRef](#)] [[PubMed](#)]
23. Ding, X.G.; Liow, C.H.; Zhang, M.X. Surface plasmon resonance enhanced light absorption and photothermal therapy in the second near-infrared window. *J. Am. Chem. Soc.* **2014**, *136*, 15684–15693. [[CrossRef](#)] [[PubMed](#)]
24. Bharathiraja, S.; Moorthy, M.S.; Manivasagan, P.; Seo, H.; Lee, K.D.; Oh, J. Chlorin e6 conjugated silica nanoparticles for targeted and effective photodynamic therapy. *Photodiagn. Photodyn. Therapy* **2017**, *19*, 212–220. [[CrossRef](#)] [[PubMed](#)]
25. Ju, Q.; Tu, D.T.; Liu, Y.S.; Li, R.F.; Zhu, H.M.; Chen, J.C.; Chen, Z.; Huang, M.D.; Yu, X. Amine-functionalized lanthanide-doped KGdF<sub>4</sub> nanocrystals as potential optical/magnetic multimodal bioprobes. *J. Am. Chem. Soc.* **2012**, *134*, 1323–1330. [[CrossRef](#)] [[PubMed](#)]
26. Yin, D.D.; Wang, C.C.; Ouyang, J.; Song, K.L.; Liu, B.; Cao, X.Z.; Zhang, L.; Han, Y.L.; Long, X.; Wu, M.H. Enhancing upconversion luminescence of NaYF<sub>4</sub>:Yb/Er nanocrystals by Mo<sup>3+</sup> doping and their application in bioimaging. *Dalton Trans.* **2014**, *43*, 12037–12043. [[CrossRef](#)] [[PubMed](#)]
27. Luo, Y.; Du, S.N.; Zhang, W.; Liao, Z.F.; Zuo, F.; Yang, S.T. Core@shell Fe<sub>3</sub>O<sub>4</sub>@Mn<sup>2+</sup>-doped NaYF<sub>4</sub>:Yb/Tm nanoparticles for triple-modality T<sub>1</sub>/T<sub>2</sub>-weighted MRI and NIR-to-NIR upconversion luminescence imaging agents. *RSC Adv.* **2017**, *7*, 37929–37937. [[CrossRef](#)]
28. Shen, J.; Sun, L.D.; Zhang, Y.W.; Yan, C.H. Superparamagnetic and upconversion emitting Fe<sub>3</sub>O<sub>4</sub>/NaYF<sub>4</sub>:Yb,Er hetero-nanoparticles via a crosslinker anchoring strategy. *Chem. Commun.* **2010**, *46*, 5731–5733. [[CrossRef](#)] [[PubMed](#)]
29. Mi, C.C.; Zhang, J.P.; Gao, H.Y.; Wu, X.L.; Wang, M.; Wu, Y.F.; Di, Y.Q.; Xu, Z.R.; Mao, C.B.; Xu, S.K. Multifunctional nanocomposites of superparamagnetic (Fe<sub>3</sub>O<sub>4</sub>) and NIR-responsive rare earth-doped up-conversion fluorescent (NaYF<sub>4</sub>:Yb,Er) nanoparticles and their applications in biolabeling and fluorescent imaging of cancer cells. *Nanoscale* **2010**, *2*, 1141–1148. [[CrossRef](#)] [[PubMed](#)]
30. Serena, A.; Corr, Y.P.; Rakovich, Y.K.; Gun, K. Multifunctional magnetic-fluorescent nanocomposites for biomedical applications. *Nanoscale Res. Lett.* **2008**, *3*, 87–104. [[CrossRef](#)]
31. Tian, G.; Gu, Z.J.; Zhou, L.J.; Yin, W.Y.; Liu, X.X.; Yan, L.; Jin, S.; Ren, W.L.; Xing, G.M.; Li, S.J.; et al. Mn<sup>2+</sup> dopant-controlled synthesis of NaYF<sub>4</sub>:Yb/Er upconversion nanoparticles for in vivo imaging and drug delivery. *Adv. Mater.* **2012**, *24*, 1226–1231. [[CrossRef](#)] [[PubMed](#)]
32. Reddy, K.L.; Rai, M.; Prabhakar, N.; Arppe, R.; Rai, S.B.; Singh, S.K.; Rosenholm, J.M.; Krishnan, V. Controlled synthesis, bioimaging and toxicity assessments in strong red emitting Mn<sup>2+</sup> doped NaYF<sub>4</sub>:Yb<sup>3+</sup>/Ho<sup>3+</sup> nanophosphors. *RSC Adv.* **2016**, *6*, 53698–53704. [[CrossRef](#)]
33. Hu, D.; Chen, M.; Gao, Y.; Li, F.Y.; Wu, L.M. A facile method to synthesize superparamagnetic and up-conversion luminescent NaYF<sub>4</sub>:Yb,Er/Tm@SiO<sub>2</sub>@Fe<sub>3</sub>O<sub>4</sub> nanocomposite particles and their bioapplication. *J. Mater. Chem.* **2011**, *21*, 11276–11282. [[CrossRef](#)]
34. Xu, X.; Lei, P.P.; Dong, L.L.; Liu, X.L.; Su, Y.; Song, S.Y.; Feng, J.; Zhang, H.J. Rational design of Nd<sup>3+</sup>-sensitized multifunctional nanoparticles with highly dominant red emission. *Dalton Trans.* **2016**, *45*, 8440–8446. [[CrossRef](#)] [[PubMed](#)]
35. He, F.; Li, C.X.; Zhang, X.Y.; Chen, Y.Y.; Deng, X.R.; Liu, B.; Hou, Z.Y.; Huang, S.S.; Jin, D.Y.; Lin, J. Optimization of upconversion luminescence of Nd<sup>3+</sup>-sensitized BaGdF<sub>5</sub>-based nanostructures and their application in dual-modality imaging and drug delivery. *Dalton Trans.* **2016**, *45*, 1708–1716. [[CrossRef](#)] [[PubMed](#)]
36. Zhou, J.; Liu, Z.; Li, F.Y. Upconversion nanophosphors for small-animal imaging. *Chem. Soc. Rev.* **2012**, *41*, 1323–1349. [[CrossRef](#)] [[PubMed](#)]

37. Xia, L.; Kong, X.G.; Liu, X.M.; Tu, L.P.; Zhang, Y.L.; Chang, Y.L.; Liu, K.; Shen, D.Z.; Zhao, H.Y.; Zhang, H. An upconversion nanoparticle–Zinc phthalocyanine based nanophotosensitizer for photodynamic therapy. *Biomaterials* **2014**, *35*, 4146–4156. [[CrossRef](#)] [[PubMed](#)]
38. Joshi, P.; Ahmadov, T.O.; Wang, P.; Zhang, P. Singlet oxygen generation under NIR light and visible light excitations of photosensitizers on upconversion nanoparticle surface. *RSC Adv.* **2015**, *5*, 67892–67895. [[CrossRef](#)]
39. Zhao, Z.; Han, Y.; Lin, C.; Hu, D.; Wang, F.; Chen, X.L.; Chen, Z.; Zheng, N.F. Multifunctional core–shell upconverting nanoparticles for imaging and photodynamic therapy of liver cancer cells. *Asian J. Chem.* **2012**, *7*, 830–837. [[CrossRef](#)] [[PubMed](#)]
40. Collins, H.A.; Khurana, M.; Moriyama, E.H.; Mariampillai, A.; Dahlstedt, E.; Balaz, M.; Kuimova, M.K.; Drobizhev, M.; Yang, V.X.D.; Phillips, D.; et al. Blood-vessel closure using photosensitizers engineered for two-photon excitation. *Nat. Photonics* **2008**, *2*, 420–424. [[CrossRef](#)]
41. Wang, D.; Zhu, L.; Pu, Y.; Wang, J.X.; Chen, J.F.; Dai, L.M. Transferrin-coated magnetic upconversion nanoparticles for efficient photodynamic therapy with near-infrared irradiation and luminescence bioimaging. *Nanoscale* **2017**, *9*, 11214–11221. [[CrossRef](#)] [[PubMed](#)]
42. Fowleya, C.; Nomikoub, N.; McHalea, A.P.; McCaughana, B.; Callan, J.F. Extending the tissue penetration capability of conventional photosensitisers: A carbon quantum dot–protoporphyrin IX conjugate for use in two-photon excited photodynamic therapy. *Chem. Commun.* **2013**, *49*, 8934–8936. [[CrossRef](#)] [[PubMed](#)]



© 2018 by the authors. Licensee MDPI, Basel, Switzerland. This article is an open access article distributed under the terms and conditions of the Creative Commons Attribution (CC BY) license (<http://creativecommons.org/licenses/by/4.0/>).